Modeling, simulation and optimization of a no-chamber solid oxide fuel cell operated with a flat-flame burner

Marcel Vogler [a,b,*], Michio Horiuchi [c], Wolfgang G. Bessler [a,b]

[a] German Aerospace Center (DLR), Institute of Technical Thermodynamics, Pfaffenwaldring 38-40, 70569 Stuttgart, Germany
[b] Universität Stuttgart, Institute of Thermodynamics and Thermal Engineering (ITW), Pfaffenwaldring 6, 70550 Stuttgart, Germany
[c] Shinko Electric Industries, 38 Kitaowaribe, Nagano 381-0014, Japan

ABSTRACT

A detailed computational model of a direct-flame solid oxide fuel cell (DFFC) is presented. The DFFC is based on a fuel-rich methane–air flame stabilized on a flat-flame burner and coupled to a solid oxide fuel cell (SOFC). The model consists of an elementary kinetic description of the premixed methane–air flame, a stagnation-point flow description of the coupled heat and mass transport within the gas phase, an elementary kinetic description of the electrochemistry, as well as heat, mass and charge transport within the SOFC. Simulated current–voltage characteristics show excellent agreement with experimental data published earlier (Kronemayer et al., 2007 [10]). The model-based analysis of loss processes reveals that ohmic resistance in the current collection wires dominates polarization losses, while electronic loss currents in the mixed conducting electrolyte have only little influence on the polarized cell. The model was used to propose an optimized cell design. Based on this analysis, power densities of above 200 mW cm^{-2} can be expected.

© 2010 Elsevier B.V. All rights reserved.

1. Introduction

The driving force for energy conversion in a solid oxide fuel cell (SOFC) is a gradient in the chemical potential of oxygen. To establish this gradient, the anode and cathode gas streams are usually separated from each other. This makes the system complex, as high-temperature sealing techniques are needed and means of thermal management have to be integrated. The separation of gas streams may be omitted by using specialized catalyst materials for the anode and cathode, making them selective for either the fuel or the oxidant. These systems are known as single-chamber fuel cells and have been widely investigated [1–3]. Still, these systems are operated inside a chamber and effort has to be made to constantly supply heat and fuel.

An even simpler, "no-chamber" setup can be conceived when exposing the cathode of a free-standing fuel cell to ambient air while continuously supplying the anode with a hot gas stream of low oxygen concentration. Such a gas stream can be easily provided by a fuel-rich flame. This leads to the concept of the direct-flame solid oxide fuel cell (DFFC). Here, the chemical gradient is built up by a fuel-rich combustion of a hydrocarbon fuel on the anode side

of the SOFC, where the combustion process consumes nearly all of the oxygen and additionally acts as a fuel reformer and heat source for the SOFC. The SOFC runs on H_2 and CO present in the flame exhaust gas. The production of hydrogen using fuel-rich flames was demonstrated by several authors mostly using catalytic combustion [4–6]. The approach of directly coupling a free-burning flame to an SOFC was first published by Horiuchi et al. [7,8]. It was subsequently investigated using different fuels and different combustion concepts [9–12].

The properties, advantages and drawbacks of DFFCs have been discussed before [10]. One problem is the inherently low electrical efficiency resulting from a conversion of a large part of the fuel's energy to heat during combustion. Moreover, previous experiments [9,10] have identified cell temperature to be of key importance for the system. In particular, the power density was found to have a maximum at around 900 K independently of the fuel used. This was attributed to the properties of the mixed-conducting electrolyte (samaria-doped ceria, SDC) used in these studies.

In order to increase DFFC efficiency, a detailed understanding of the factors governing DFFC performance is required, in particular in the light of the observed strong and nonlinear temperature influence. However, this is a difficult task because of the chemical and thermal complexity of a DFFC, where flame and fuel cell are inherently coupled. In the present study, we use modeling and simulation techniques to identify and reduce efficiency losses and improve DFFC performance. A detailed model accounting for the full coupling of fuel cell and flame is developed, comprising all

relevant chemical, physical and transport processes. The model allows a detailed insight into the DFFC system, but comes at high computational cost. A reduced model is therefore developed that strongly reduces computational time. The reduced model is used to predict optimum working conditions and design parameters for increasing electrical efficiency of the DFFC.

2. Modeling and simulation

2.1. Model structure

The model described in this section represents the experimental setup by Kronemayer et al. [10]. An SOFC is placed in the exhaust of a flat-flame burner. Fig. 1 shows the experimental setup along with a sketch of the modeling domain. Experimentally the cathode temperature and the current–voltage relation (*IV* curve) of the fuel cell were recorded. However, important parameters governing fuel cell performance include gas composition of anode and cathode, temperature distribution throughout the cell, as well as material parameters (e.g., resistivities of the used materials, porosity of the electrodes, etc.), are only accessible via simulations. The model consists of two main parts which we focus on in the remainder of this section: Firstly the flame itself has to be modeled in order to determine gas-phase composition and temperature at the surface of the fuel cell anode. Secondly the temperature-dependent electrochemical processes of the fuel cell have to be modeled in order to predict the power output of the system.

Depending on the focus of the analysis, different levels of model detail will be used. Whenever possible the model complexity will be reduced to enable faster computations. To ensure adequate reproduction of crucial system properties, the reduced model is compared to the full model. This section presents the full model, while model reduction will be discussed in Section 3.3.

All model equations are summarized in Table 1 . The equation numbers given in the following subsections refer to this table. All model parameters are summarized in Table 2. Full and reduced models are implemented in the in-house software DENIS (Detailed Electrochemistry and Numerical Impedance Simulation) [13]. For numerical simulations, the 1D computational domain was discretized into 50 grid points using finite-volume techniques.

2.2. Flame and gas phase

A reactive non-isothermal stagnation point flow model [14,15] is used to describe the flat-flame burner (Table 1, Eqs. (1)–(6)). This model represents an exact 1D solution of the Navier–Stokes equations accounting for the full coupling of heat and mass transport in the anode gas phase. The combustion chemistry is described by an elementary kinetic reaction mechanism [16]. We use GRI-Mech 3.0 [17], a mechanism optimized for the simulation of natural gas combustion. The use of methane instead of natural gas allows the reduction of the reaction mechanism to hydrocarbon species smaller than C_3H_4 [16]. Furthermore, because we are not interested in pollution chemistry, nitrogen–oxygen species and their reactions are omitted. The resulting mechanism used for the present study consists of 220 homogeneous gas-phase reactions between 36 species (CH_4, H_2, H_2O, N_2, O_2, O, H, OH, HO_2, H_2O_2, CO, CO_2, CH, HCO, $CH_2^{triplet}$, $CH_2^{singlet}$, CH_2O, CH_3, CH_3O, CH_2OH, CH_3OH, C, C_2H, C_2H_2, C_2H_3, C_2H_4, C_2H_5, C_2H_6, HCCO, CH_2CO, HCCOH, C_3H_7, C_3H_8, CH_2CHO, CH_3CHO, N_2).

For the cathode a constant non-reactive gas atmosphere of N_2:O_2 = 79:21 was assumed. The pressure was set to 1 bar.

2.3. Fuel cell electrolyte

A samarium-doped ceria (SDC) electrolyte was used in the experiments by Kronemayer et al. [10]. Over the whole range of experimental conditions, SDC is a mixed ionic and electronic conductor [18]. Ionic and electronic resistivity are functions of temperature (Eqs. (39) and (40)). The temperature dependence of the ionic conductivity was measured by the cell manufacturer (Shinko Electric Industries [7]) using AC impedance spectroscopy in air between 550 K and 700 K. For the electronic conductivity as well as additional data for the ionic conductivity at higher temperatures fits of Eqs. (39) and (40) to published experimental data were performed.

Electronic conduction results in an electrical current short-circuiting anode and cathode. This is potentially a major loss mechanism for fuel cell performance. The electronic loss current is calculated using Eq. (38) according to the model by Riess and Gödickemeier [19,20] as reformulated by Hao and Goodwin [21].

2.4. Fuel cell electrodes

The electrodes consist of three phases: the porous gas phase and the two solid phases of the mixed-conducting electrolyte and electronically conducting electrode. Chemistry within the porous electrodes is dominated by surface reactions. Therefore we treat the gas phase as chemically non-reactive. Gas transport in the pores is described by coupled multi-component diffusion and Darcy porous flow (Eqs. (7)–(12)). A detailed elementary kinetic model is used to describe the heterogeneous surface chemistry. The reaction mechanism used to calculate the chemical source terms (Eq. (13)) for the electronically conducting phase of the anode was developed for reforming, shift and partial oxidation of methane on nickel surfaces [22]. It consists of 42 reactions between 6 gas-phase species (H_2, CO, H_2O, CO_2, CH_4, O_2) and 12 surface species (H, OH, H_2O, O, CH_4, CO, CO_2, CH, CH_3, CH_2, C, free Ni sites). As the reaction mechanism for the heterogeneous chemistry on the SDC surface is unknown, a reaction mechanism developed previously for YSZ [23] is used, consisting of four reactions between one gas-phase species (H_2O), four surface-adsorbed species (H_2O, OH^-, O^{2-}, free sites) and two bulk species ($O_O^\times$, $V_O^{\bullet\bullet}$).
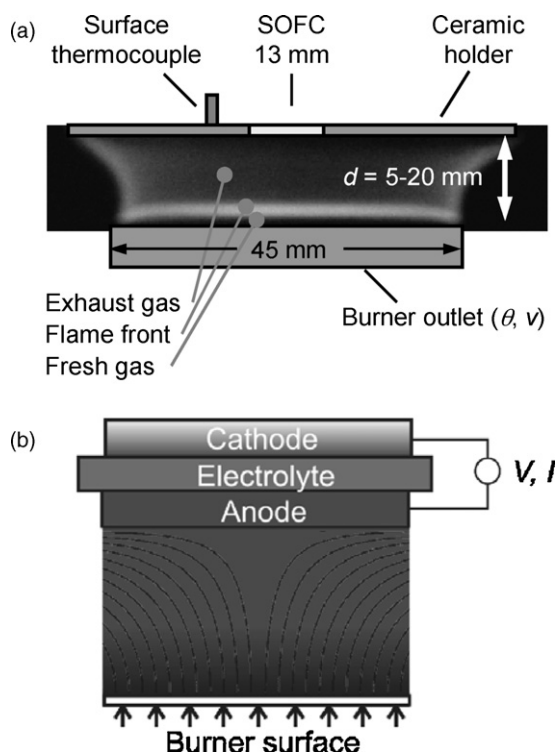

Fig. 1. Experimental setup (a) and sketch of the modeling domain (b).

Table 1
Summary of all model equations. See [14] for a definition of symbols and their units.

Process	Model equation	
Reactive stagnation point flow		
Mass continuity	$\dfrac{\partial \rho}{\partial t} = -\dfrac{\partial(\rho \upsilon_y)}{\partial y} - 2\rho V$	(1)
Radial momentum	$\dfrac{\partial(\rho V)}{\partial t} = -\dfrac{\partial(\rho \upsilon_y V)}{\partial y} - \dfrac{\partial}{\partial y}\left(\mu \dfrac{\partial V}{\partial y}\right) - \rho V^2 - \Lambda$	(2)
Species conservation	$\dfrac{\partial(\rho Y_i)}{\partial t} = -\dfrac{\partial(\rho \upsilon_y Y_i)}{\partial y} - \dfrac{\partial j_i^{\text{diff}}}{\partial y} + \dot{s}_i^V M_i$	(3)
Energy conservation	$\dfrac{\partial(\rho c_P T)}{\partial t} = -\dfrac{\partial(\rho \upsilon_y c_P T)}{\partial y} + \dfrac{\partial}{\partial y}\left(\lambda_q \dfrac{\partial T}{\partial y}\right) - \displaystyle\sum_{i \in S_g} c_{P,i} j_i^{\text{diff}} \dfrac{\partial T}{\partial y} - \displaystyle\sum_{i \in S_g} \dot{s}_i^V h_i$	(4)
Radial pressure	$\dfrac{\partial \Lambda}{\partial y} = 0$	(5)
Species production by homogeneous chemistry	$\dot{s}_i^V = \displaystyle\sum_m v_{i,m} \left(k_{f,m} \displaystyle\prod_{j \in R_{f,m}} c_j^{v_j'} - k_{r,m} \displaystyle\prod_{j \in R_{r,m}} c_j^{v_j''} \right)$	(6)
Porous gas-phase transport		
Mass transport	$\dfrac{\partial(\epsilon c_i)}{\partial t} = -\dfrac{\partial J_i^{\text{diff}}}{\partial y} - \dfrac{\partial J_i^{\text{flow}}}{\partial y} + \dot{s}_i^V$	(7)
Knudsen diffusion	$J_i^{\text{diff}} = -c_i \overline{D}_i \dfrac{\partial X_i}{\partial x}$	(8)
Darcy flow	$J_i^{\text{flow}} = -X_i c_g \dfrac{B}{\mu} \dfrac{\partial p}{\partial y}$	(9)
Mixture averaged diffusion coefficient	$\overline{D}_i = (1 - X_i) \left(\displaystyle\sum_{j \in S_g, j \neq i} X_j / D_{ij}^{\text{eff}} \right)^{-1}$	(10)
Bosanquel diffusion coefficients	$D_{ij}^{\text{eff}} = D_{ji}^{\text{eff}} = \dfrac{\epsilon}{\tau} \dfrac{1}{2} \left(\dfrac{1}{(1/D_i^{\text{K}}) + (1/D_{ij})} + \dfrac{1}{(1/D_j^{\text{K}}) + (1/D_{ij})} \right)$	(11)
Kozeny–Carman relation	$B = \dfrac{\epsilon^2 d_P^2}{72 \cdot \tau(1 - \varepsilon)^2}$	(12)
Volumetric gas-phase production rate	$\dot{s}_i^V = \displaystyle\sum_{k \in S_N} A_k^V \dot{s}_i^A$	(13)
Heat transport MEA		
Energy conservation	$\dfrac{\partial(\rho c_P T)}{\partial t} = \dfrac{\partial}{\partial y}\left(\lambda_q \dfrac{\partial T}{\partial y}\right) + \dot{s}_q$	(14)
Heat sources	$\dot{s}_q = \sigma_{\text{elyt}}^i \left(\dfrac{\partial \phi_{\text{elyt}}}{\partial y} \right)^2 + \displaystyle\sum_{i \in S_g, S_s} \dot{s}_i^V h_i$	(15)
Heat transfer coefficient	$\alpha = Nu \cdot \dfrac{\lambda_q^{\text{air}}}{L_{\text{char}}}$	(16)
Surface heat radiation	$j_q^{\text{elec}} = \alpha(T_{\text{elec}} - T_{\text{gas}}) + \sigma_{\text{SB}} \in_q (T_{\text{elec}}^4 - T_{\text{ref}}^4)$	(17)
Heterogeneous chemistry model		
Surface coverages	$\theta_i = \dfrac{c_i}{\Gamma_k}$	(18)
Chemistry source terms	$\dot{s}_i^A = \displaystyle\sum_m v_{i,m} \left(k_{f,m} \displaystyle\prod_{j \in R_{f,m}} c_j^{v_j'} - k_{r,m} \displaystyle\prod_{j \in R_{r,m}} c_j^{v_j''} \right)$	(19)
Forward reaction rate constant	$k_{f,m} = k_{f,m}^0 \cdot T^{\beta m} \cdot \exp\left(-\dfrac{E_{f,m}^{\text{act}}}{RT} \right)$	(20)
Reverse reaction rate constant	$k_{r,m} = k_{f,m} \cdot \exp\left(\dfrac{\Delta G_m}{RT} \right)$	(21)
Gibbs free reaction enthalpy	$\Delta G_m = \displaystyle\sum_{i \in R_{f,m}} v_{i,m}'(h_i - T \cdot s_i) - \displaystyle\sum_{i \in R_{r,m}} v_{i,m}''(h_i - T \cdot s_i)$	(22)
Electrochemistry anode		
Forward charge-transfer reaction rate constant	$k_{f,\text{ct}} = k_{f,\text{ct}}^0 \exp\left(-\dfrac{E_{f,\text{ct}}^{\text{act}}}{RT} \right) \exp\left(\alpha \dfrac{zF}{RT} \cdot \Delta\phi_{\text{an}} \right)$	(23)
Reverse charge-transfer reaction rate constant	$k_{r,\text{ct}} = k_{f,\text{ct}} \exp\left(\dfrac{\Delta G_m}{RT} \right) \exp\left(-(1-\alpha)\dfrac{zF}{RT} \cdot \Delta\phi_{\text{an}} \right)$	(24)
Total volumetric current	$i_{\text{tot}}^V = \displaystyle\sum_{j \in \text{CTRs}} i_j^V$	(25)
Faradaic current of single charge-transfer reaction	$i_{\text{CTR}}^V = zF l_{\text{TPB}}^V \left(k_f \displaystyle\prod_{j \in R_{f,\text{ct}}} \theta_j^{v_j'} - k_r \displaystyle\prod_{j \in R_{r,\text{ct}}} \theta_j^{v_j''} \right)$	(26)

Table 1 (*Continued*)

Process	Model equation	
Electrochemistry cathode		
Exchange current density	$i_{ca}^0 = i_{ca}^* \exp\left(-\dfrac{E_{cath}^{act}}{RT}\right) \left(\dfrac{p_{O_2}^{ca}}{p_{O_2}^*}\right)^{1/4} \left(1 + \dfrac{p_{O_2}^{ca}}{p_{O_2}^*}\right)^{-1/2}$	(27)
Faraday current cathode	$i_{ca} = i_{ca}^0 \cdot \left[\exp\left(\beta_a \dfrac{zF}{RT}\eta_{ca}\right) - \exp\left(-\beta_c \dfrac{zF}{RT}\eta_{ca}\right)\right]$	(28)
Electrical properties of the MEA		
Potential SOFC	$E(i) = \phi_{elde,cath} - \phi_{elde,an}(i)$	(29)
Potential steps anode	$\Delta\phi_{an} = \phi_{elde,an} - \phi_{elyt,an}$	(30)
Potential steps cathode	$\Delta\phi_{cath} = \phi_{elde,ca} - \phi_{elyt,ca}$	(31)
Overpotential	$\eta = \Delta\phi - \Delta\phi_{equil}$	(32)
Potential distribution electrode	$\dfrac{\partial}{\partial y}\phi_{elde} = 0$	(33)
Potential distribution dense electrolyte	$\dfrac{\partial}{\partial y}\left(\sigma_{elyt}\dfrac{\partial}{\partial y}\phi_{elyt}\right) = 0$	(34)
Potential distribution composite electrode	$\dfrac{\partial}{\partial y}\left(\sigma_{elyt}f_\sigma \dfrac{\partial}{\partial y}\Delta\phi_{an}\right) = -i_{tot}^V$	(35)
Total current	$i = \int i_{tot}^V dy + i_{el}$	(36)
Ionic current density	$i_{elyt} = -\sigma_{elyt}^{eff}\dfrac{\partial}{\partial y}\phi_{elyt} = -\sigma_{elyt}f_\sigma \dfrac{\partial}{\partial y}\phi_{elyt}$	(37)
Electronic current of mixed conducting electrolyte	$i_{el} = -i_{elyt}\dfrac{\sigma_{elyt}^e(p_{O_2}^{ca}, T)}{\sigma_{elyt}^i(T)}\exp\left(\dfrac{\eta_{ca}F}{RT}\right)\cdot\dfrac{\exp(EF/RT) - 1}{1 - \exp((-i_{elyt}L_{elyt}F)/(RT\sigma_{elyt}^i))}$	(38)
Electrolyte electronic conductivity	$\sigma_{elyt}^e(p_{O_2}^{cath}, T) = \left(\dfrac{p_{O_2}^{cath}}{p^0}\right)^{-1/4}\cdot\dfrac{a_0^{elyt}}{T}\cdot\exp\left(\dfrac{b_0^{elyt}}{T}\right)$	(39)
Electrolyte ionic conductivity	$\sigma_{elyt} = \dfrac{A_\sigma}{T}\cdot\exp\left(-\dfrac{E_\sigma}{RT}\right)$	(40)
Resistance of Pt wire	$R_a = \rho_{con}\cdot\dfrac{i_{con}}{A_{con}}$	(41)
Specific resistance of the Pt wire	$\rho_{con} = \rho_{con}^0\cdot(1 + \alpha_{con}\cdot(T - T_0))$	(42)

The charge-transfer reactions on anode and cathode are assumed to take place at the three-phase boundary distributed over the whole volume of the electrodes. For the anode, an elementary kinetic mechanism is used based on a hydrogen spillover mechanism (Eqs. (23)–(26)) [23]. For the cathode, the modified Butler–Volmer ansatz (Eqs. (27)–(28)) developed by Zhu et al. [24] is used.

Thermal management of the SOFC is modeled by including heat production by heterogeneous chemistry in the anode, Joule heating and heat conduction through the entire SOFC, as well as radiative and convective heat transport at the electrode surfaces (Eqs. (14)–(17)).

2.5. Connecting wires

In the experiments the SOFC was connected via platinum wires to the measuring device. The wire had a diameter of 0.3 mm and a total length of 60 mm. The wire was attached to a platinum mesh embedded into the electrodes as current collector. The mesh is the same high temperature as the SOFC; the wire passes through the hot flame regions and may be partially even hotter. The ohmic resistance of wire and mesh are temperature dependent via Eq. (42). In the model we include a 60-mm wire at SOFC temperature. It adds to the overall ohmic resistance of the system and will be shown to have a large influence on the performance.

2.6. Model validation and parameter estimation

Model validation is a key requirement for performing reliable optimization studies. Simulation targets for model validation have to be experimentally available physical data which the model has to predict correctly after an adjustment of unknown model parameters. Because the model is based on physicochemical fundamentals, it is expected to be valid outside the conditions covered in the validation experiment. In the experiments by Kronemayer et al. [10], the cell temperature on the cathode surface T_{cath} and current–voltage characteristics (*IV* curves) were recorded for a variety of equivalence ratios Φ and temperatures (realized by varying the burner–SOFC distances d). These flame conditions are summarized in Table 3. The experimentally identified key features of the system are summarized as follows:

- *Linearity of the IV curves*: The *IV* curves for all investigated flame conditions show a characteristic linear shape
- *Open-circuit voltage (OCV)*: The OCV is lower than the value predicted from thermodynamics
- *Peak power P_{max}*: The power output of the SOFC is small compared to the fuel available for electrochemical conversion by the SOFC (low efficiency)
- *T_{cath}*: Temperatures measured with a surface thermocouple at the cathode side of the fuel cell are low (400–700 °C) compared to expected flame temperatures (1600–1900 °C)

The only input to the simulations are the composition of the fuel given by the equivalence ratio Φ, the inlet velocity of the premixed fuel v_{inlet}, the distance between burner outlet and anodic surface of the fuel cell d, and the temperature of the water-cooled burner sinter matrix. All features listed above need to be directly predicted by the model and are ideal for model validation.

Given the complexity of the system and the level of detail it is modeled at, a large number of parameters enter the simula-

Table 2
Summarized model parameters. (a) Values fitted to experimental data provided by Shinko Electric Industries Co. Ltd. (b) Parameter was adjusted by fitting to experimental data of Kronemayer et al. [10]. (c) Estimated from SEM pictures provided by Shinko Electric Industries Co. Ltd. (d) Estimated. (e) Estimated from percolation theory [27]. (f) Material data sheet from manufacturer. (g) From the experimental setup. See [13] for a definition of symbols.

Parameter	Definition	Value	Unit	Ref.
Porous gas-phase transport				
d_{an}	Anode thickness	175	μm	(c)
ε^{an}	Anode porosity	37%	–	(c) and (e)
τ^{an}	Anode tortuosity	3.5	–	(d)
d_{cath}	Cathode thickness	250	μm	(c)
ε^{cath}	Cathode porosity	30	%	(c)
τ^{cath}	Cathode tortuosity	4	–	(d)
Electric parameters				
A_{cell}	Active cell surface	1.3	cm^2	(g)
a_0^{elyt}	Pre-exponential factor electronic conductivity of the dense electrolyte	7.3×10^{11}	K$(\Omega\,\text{m}\,\text{Pa}^{1/4})^{-1}$	[26]
b_0^{elyt}	Temperature coefficient of electronic conductivity of the dense electrolyte	2.7×10^{-4}	K	[26]
E_σ	Activation energy of the ionic conductivity	77.2	kJ	[27] and (a)
A_σ	Pre-exponential factor of ionic conductivity	5.2×10^7	K^{-1}	[27] and (a)
d_{elyt}	Electrolyte thickness	170	μm	(c)
l_{con}	Length of connecting wires	0.6	cm	(g)
A_{con}	Cross sectional area	0.28	mm^2	(f)
α_{con}	Temperature-pre-factor for contact wire resistance	3.8×10^{-3}	K^{-1}	(f)
ρ_{con}^0	Length-specific resistance of contact wire	110	$\Omega\,\text{mm}^2(\text{m}^{-1})$	(f)
Electrochemistry				
β	Symmetry factor	0.5	–	[28]
E_{cath}^{act}	Activation energy of cathodic CTR	88.6	kJ mol^{-1}	[28]
i_{ca}^*	Volumetric exchange current density	5.9×10^{11}	A m^{-3}	[28]
$p(O_2)$	Oxygen partial pressure	21.3	kPa	(g)
$l_{TPB}^{V,an}$	Volume specific length of the TPB	10^{12}	m^{-2}	(e)
k_{H1}^0	Pre-exponential factor of the CTR at the anode	135	mol s^{-1}	(b)
E_{H1}^{act}	Activation energy of the CTR at the anode	185	kJ mol^{-1}	(b)
Heat management				
L_{char}	Characteristic length	0.012	m	(g)
Nu	Nusselt number	1	–	[29]
λ_q^{air}	Heat conductivity of the ambient air	0.058	W(m K)$^{-1}$	[29]
λ_q^{elyt}	Heat conductivity of the dense electrolyte	5	W(m K)$^{-1}$	(c)
λ_q^{an}	Heat conductivity of the porous anode	8	W(m K)$^{-1}$	(c)
λ_q^{cat}	Heat conductivity of the porous cathode	10	W(m K)$^{-1}$	(c)
ε_q^{ca}	Emissivity of the cathode surface	0.75	–	[30]
ε_q^{an}	Emissivity of the anode surface	0.75	–	[30]

tions (Table 2) and not all of them are known exactly. This is either because they cannot be derived by other means than simulation (e.g., rate coefficients of the charge-transfer reactions), or because published data are not exactly applicable to the experimental conditions or the materials used (e.g., cathodic emissivity or electronic conductivity of the SDC electrolyte), or simply because they were deemed unimportant (e.g., the length of the contact wire being exposed to the hot flame exhaust). The missing or uncertain parameters have to be adjusted within physically reasonable limits so the model correctly reproduces the experimental results.

Table 3
Overview over the different flame conditions used in this study. "Std." (last row) marks the standard condition used for comparison between full model and reduced model.

No.	Φ	v_{inlet} (cm s^{-1})	d (cm)
1	1.1	10	2
2	1.1	20	2
3	1.1	30	2
4	1.2	10	2
5	1.2	20	2
6	1.2	30	2
7	1.3	10	2
8	1.3	20	2
9	1.3	30	2
10	1.4	10	2
11	1.4	20	2
Std.	1.2	10	1

3. Results and discussion

3.1. Full model

Simulations using the full model were carried out for one representative flame condition marked "Std." in Table 1. This condition was chosen because in the experiment it yielded a stable flame for all investigated fuels. Simulations were carried out for both, an unpolarized and a polarized cell. Fig. 2 summarizes the results that are discussed in the following.

Fig. 2a shows the calculated current–voltage curve and power density including a comparison to experimental data [10] under the same operating conditions. The agreement between experiment and simulation is excellent (i.e. 1.5% at P_{max}) with a maximum deviation occurring at OCV, where the cell voltage is overpredicted by 5%. This discrepancy will be further discussed below.

If no external load is connected to the fuel cell (OCV) and the system has reached a steady state, a time-independent species and temperature profile develops in the gas phase between burner and anode surface showing only spatial variations. The temperature distribution in flame and SOFC is shown in Fig. 2b. The DFFC system produces heat via the combustion chemistry. Consequently, strong temperature gradients are observed in the gas phase (right part of the plot). The peak temperature of the flame is about 1900 K which is about 300 K lower compared to an adiabatic flame of the same equivalence ratio. In contrast, the temperature distribution within the fuel cell itself (left part of the plot) is almost uniform (simulated difference between anode and cathode sur-
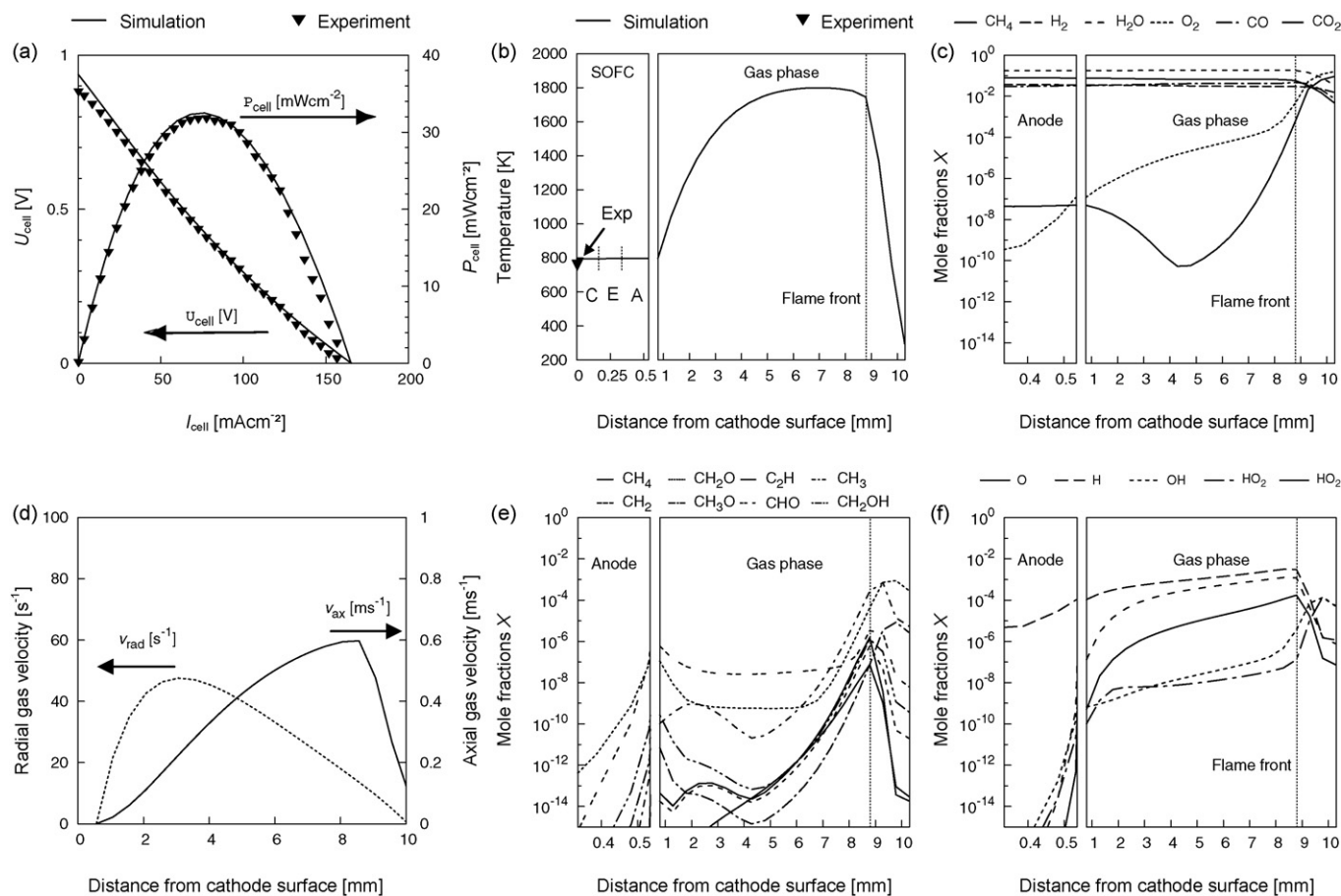
Fig. 2. Simulation results of the full model for the DFFC system at standard conditions (cf. Table 3). (a) Current–voltage and current–power behavior compared to experimental data [10]. (b) Temperature profile in the gas phase and the solid phases. (c) Major gas-phase concentration profiles. (d) Axial and scaled radial velocities. (e) Carbon radical species concentration profiles. (f) Hydrogen/oxygen radical species concentration profiles.

face: 3 K). This behavior results from the high heat conductivity of $5–10\,W(m\,K)^{-1}$ and the small thickness of the SOFC compared to the gas phase which is several mm thick and has a heat conductivity of around $0.025\,W(m\,K)^{-1}$. The figure also includes the experimentally measured temperature at the SOFC cathode, which is only slightly higher than the simulated temperature. The results show that the fuel cell thermally strongly influences the flame. Heat is led away via three mechanisms: (1) heat conduction and convection away from the cathode surface; (2) heat conduction from the gas phase to the cooled burner matrix; (3) radiation from both SOFC surfaces. Thus, the SOFC and the flame are thermally strongly coupled.

The species profiles in the gas phase (Fig. 2c, e, and f) are highly nonlinear, resulting from the coupled transport, reaction kinetics, and thermodynamical properties. For example, when going from the burner outlet towards the SOFC, the methane mole fraction strongly decreases to 10^{-10} as it is consumed through gas-phase flame chemistry. As the gas mixture rapidly cools down on its way towards the anode, further reactions establish a value around 10^{-5} which is close to the equilibrium concentration. Other main species (H_2O, H_2, CO, CO_2) show only little variation once behind the flame front. The radical species peak at the flame front, which is typical for flames, and then follow their respective kinetic and thermodynamic properties when the gas cools down. The flame, judged by the concentration profiles of oxygen and methane, extends roughly about 1 cm from the burner outlet in the direction of the fuel cell which is in good agreement with free flames [16]. The concentration of the radical species strongly decreases inside the porous

structure of the anode as they undergo heterogeneous reactions with the catalytically active anode surface forming stable gas-phase species.

The axial and scaled radial velocities of the stagnation point flow field [15] are shown in Fig. 2d. The axial velocity has a maximum close to the position of the flame front and decreases until it is zero at the SOFC surface.

3.2. Electrochemically active species

When current is drawn from the cell, oxygen ions from the cathode move through the electrolyte and oxidize the fuel on the anode side. In principle any species at the anode side that can be oxidized may serve as a fuel. To determine the main electrochemically active species of the DFFC system, calculations of the SOFC under electrical load (150 mA) are further compared to OCV conditions. The value of 150 mA was chosen because it is the maximum current which could be drawn from the cell experimentally at the standard conditions and hence the effect on surface coverage and gas-phase concentration will be the strongest.

Fig. 3 shows concentration profiles of the gas-phase species inside the porous anode and in the gas volume between anode and burner outlet for selected species at OCV (0 mA) and at 150 mA electrical load. Methane and oxygen (Fig. 3a) rapidly decrease from their inlet concentrations at $\Phi = 1.2$ close to the burner outlet as they are consumed by the flame. At the same time, radical species are produced (OH, H, CH). Polarization shows hardly any effect on the concentration of any of the species (note the logarithmic
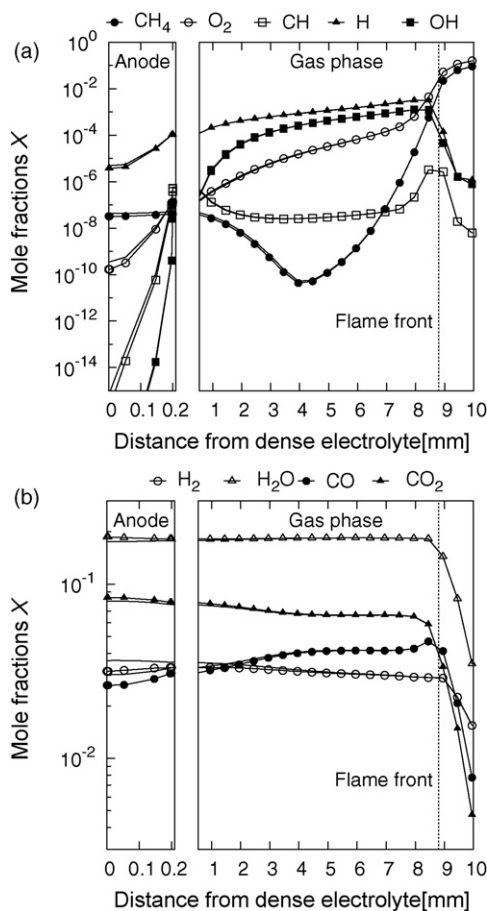
Fig. 3. Comparison of concentration profiles of selected gas-phase species in the porous anode and the gas phase calculated for OCV (solid lines) and for 150 mA electrical load (lines with symbols).

Fig. 4. Comparison of simulated current–voltage (a) and power–current (b) behavior of full and reduced models with experimental data [10].

scale). All flame radicals have an overall low concentration inside the porous anode.

In Fig. 3b the potential fuel species (H_2, CO) and their products (H_2O, CO_2) are plotted. Concentrations of both fuel species decrease by a comparable magnitude when the cell is polarized. This shows that both H_2 and CO are electrochemically active, either directly or indirectly via water–gas shift reactions. The concentrations of all species under polarization converge against their respective values at OCV close to the flame front. Thus, the fuel cell consumes only a small fraction of the partially oxidized fuel supplied by the flame, and most of the H_2 and CO leaves the system unused. Products of the electrochemical conversion taking place inside the SOFC do not influence the flame. The flame and the SOFC are chemically decoupled.

3.3. Model reduction

The full model is detailed but computationally costly and therefore not suitable for parameter studies or optimization. The simulation of the complex flame chemistry is by far the most time-consuming aspect of the model. On the other hand, as discussed in Section 3.2, flame and SOFC are chemically decoupled. The decoupling can be exploited by assuming a constant gas-phase composition just above the SOFC anode. To account for the different burner operating conditions and the accordingly different gas compositions, the concentration of gas-phase species is set to the respective values calculated using the full model. Furthermore, the
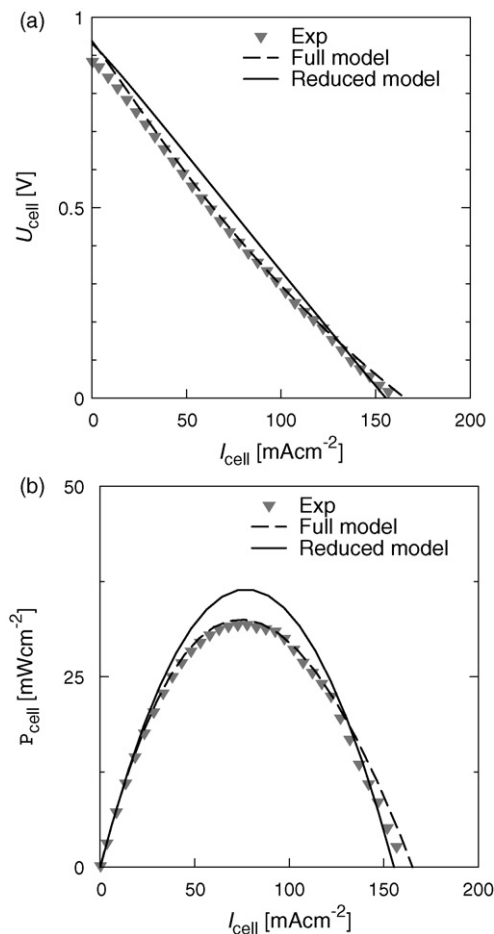
simulations using the full model predict a temperature variation of only 3 K over the thickness of the SOFC. Compared to the temperature gradient of roughly 1000 K in the gas phase, the temperature gradient inside the fuel cell is negligible. Consequently, isothermal conditions are assumed, and the temperature is set constant to the experimentally determined value of the cathode surface.

The predicted polarization characteristics of full and reduced models are compared in Fig. 4 for standard conditions (Table 1). The OCV and maximum power density of the two models differ by only 10%, which is a very good agreement given the strong simplifications made. The shape of the IV curve is almost identical. Therefore, the main experimental features are reproduced correctly by the reduced model. Consequently, it will be used in the following for model validation and parameter studies.

Note that the calculation of an IV curve consisting of 100 points between open circuit and closed circuit takes roughly 6 h using the full model. This could be reduced to about 10 min when calculations are performed with the reduced model.

3.4. Model validation over wide range of experimental conditions

Fig. 5 shows how the predictions of the reduced model compare to the measured current–voltage dependencies for the various experimental flame conditions shown in Table 1. For all conditions, simulation and experiment show a nearly linear relationship between current and cell voltage. This indicates that the system is, even at high currents, not limited by transport processes. The
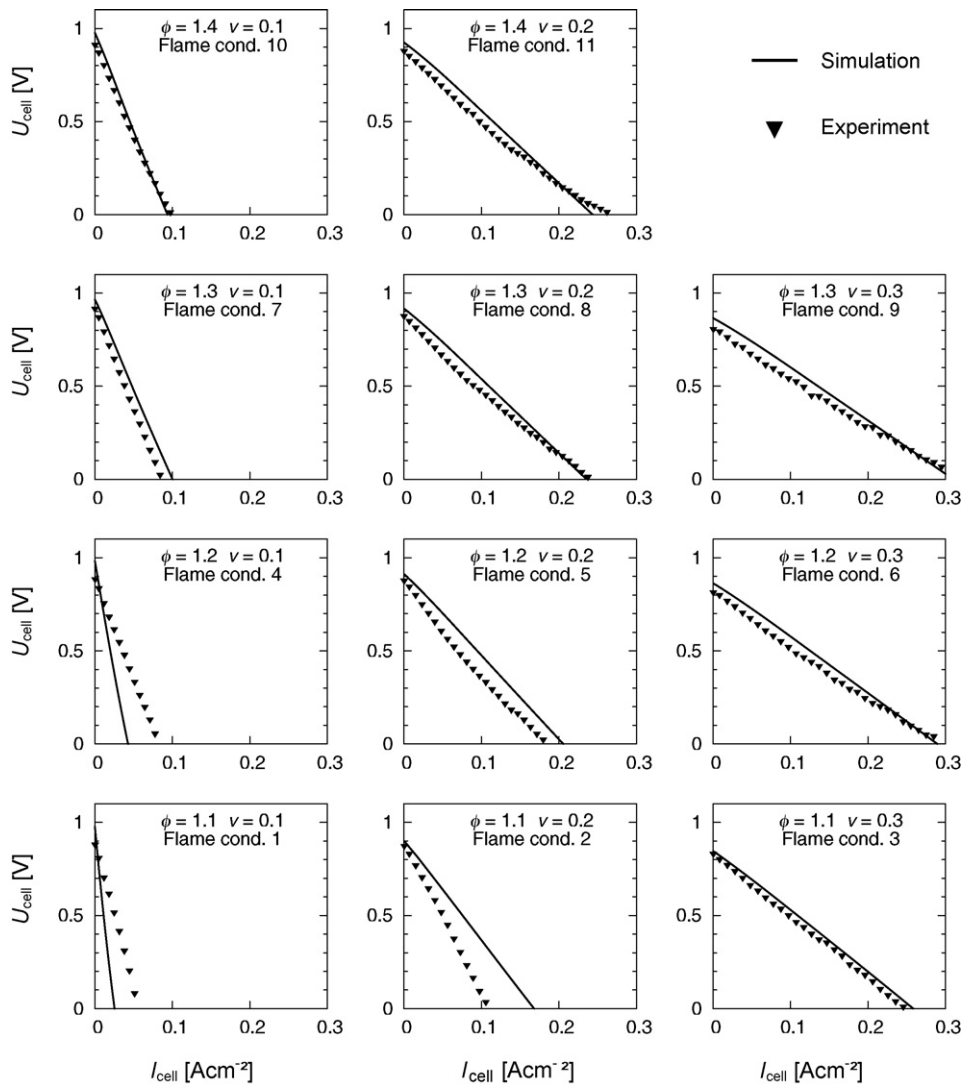
Fig. 5. Comparison of reduced model predictions of current–voltage curves with experimental data [10] for all investigated flame conditions (see Table 1).

model predictions show a good agreement with the experiment except for conditions of low equivalence ratio Φ and low inflow velocity v_{inlet} (conditions 1, 2, 4, 5). The origin of this discrepancy is unclear.

For further discussion, the maximum power output P_{max} and the OCV are plotted versus flame condition in Fig. 6. Both, the predicted and experimentally measured OCV decrease for constant equivalence ratio with increasing fuel inlet velocities. As shown in Fig. 6a, the model generally overpredicts the OCV. This is not a problem of the reduced model as the full model shows this behavior as well (Fig. 2a). Three reasons for this systematic overprediction are possible. Firstly, in the experimental setup the flame exhaust may alter the cathodic gas composition as it flows around the sample holder. This would result in lower OCV due to a lower concentration of oxygen. Calculations assuming an oxygen concentration of about 1% instead of 21% resulted in a correct prediction of the OCV. However it is deemed unlikely that the exhaust would alter the cathode gas composition to such an extent without a flame developing on the cathode side. Secondly, the electrolyte layer may not be completely gas-tight allowing the cross-over of fuel and oxidizer thereby lowering the OCV. Especially after several thermal

cycles during start-up and shut-down microcracks might be introduced in the electrolyte by thermal stress. Thirdly, the electronic conductivity of the electrolyte could be estimated too low. The coefficients for the calculation of the electronic conductivity depend on the composition of the SDC, temperature, and local oxygen concentration. Literature data had to be extrapolated to the exact material composition used in the experiments.

With respect to the maximum power output shown in Fig. 6b, the model predictions and experimental data are in good agreement. Both show an increase of system performance with increasing velocity and, for constant velocities, with increasing equivalence ratio. Generally an increase in inflow velocity of the premixed fuel results in an increase of the temperature of the SOFC. As most processes inside the SOFC are thermally activated, a performance increase with increasing temperature is expected.

3.5. Influence of temperature

Calculations using the reduced model were performed for cell temperatures ranging from 500 K to 1500 K. The resulting peak
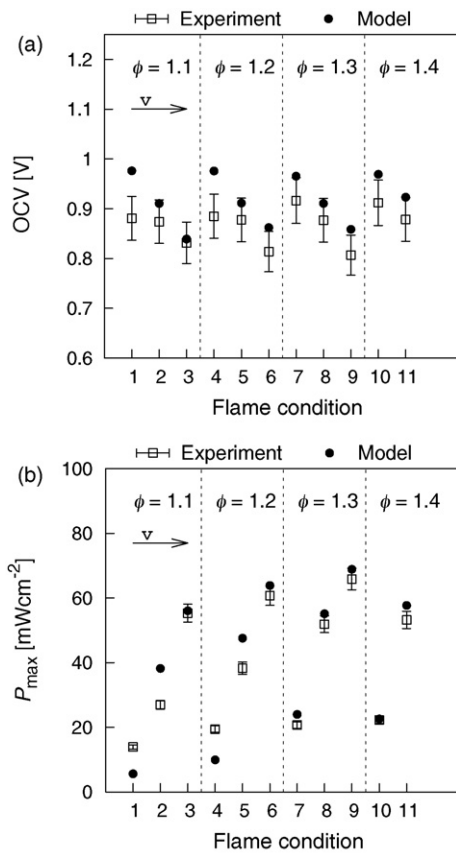
Fig. 6. Comparison of reduced model predictions of open-circuit voltage (OCV) and peak power density (P_{max}) with experimental data [10] for all investigated flame conditions (see Table 1).

Fig. 7. Simulated peak power density (P_{max}, b) and open-circuit voltage (OCV, a) versus cell temperature. Simulations are performed for standard conditions using the reduced model. The vertical lines denote the temperature of maximum peak power. The simulations are compared to experimental data from DFFC systems operated with a flat-flame burner [10] and with a porous burner [25]. Note that the porous-burner experiments were performed with different cells and are added to show the trends for higher temperatures.

power and the predicted OCV for the different temperatures are shown in Fig. 7 together with the theoretical value OCV_{Nernst} calculated from the Nernst equation under the assumption of a thermally equilibrated gas phase. The figure also shows experimental data. With a flat-flame burner, a maximum temperature of roughly 1000 K could be achieved. For higher temperatures, we used additional data from experiments with a porous burner which allows for cell temperatures up to 1400 K [25].

The experimental power densities (Fig. 7b) have a pronounced maximum at around 900–950 K. This volcano-type behavior is very well reproduced by the model. The origin of this effect will be discussed below.

The OCV (Fig. 7a) continuously decreases with increasing temperature. Again, experimental and simulated data are in good agreement. However, they are systematically below the Nernst voltage. This is caused by the electronic conductivity of the mixed conducting electrolyte. Electronic loss currents strongly increase with increasing temperature (Table 1, Eq. (38)). This causes a decrease in OCV [19,20]. For low temperatures, where electronic current becomes small, the model-predicted OCV converges against the Nernst voltage.

3.6. Analysis of loss processes

The volcano-type behavior of the DFFC's performance with respect to temperature requires specific attention. Fig. 8 shows the absolute and relative power losses as a function of temperature, where the model allows to separate the contributions of
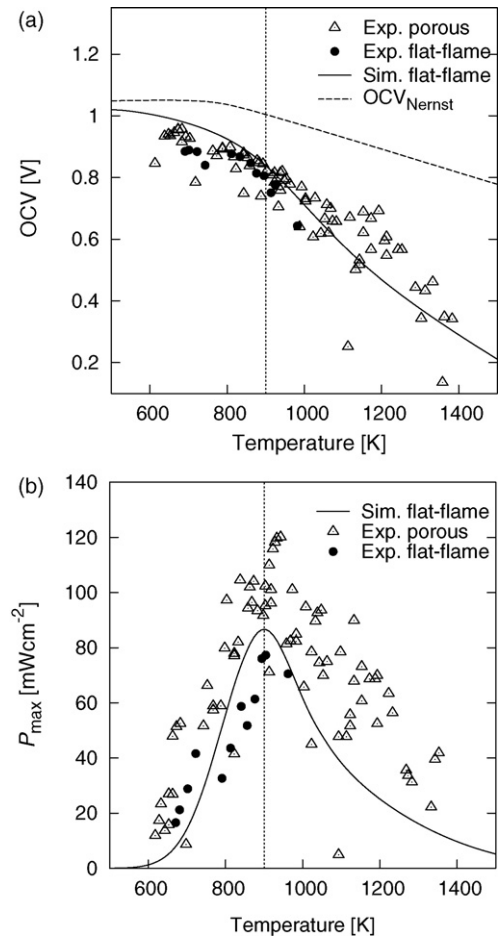
anode, cathode, electrolyte ionic resistance, electrolyte electronic loss current, and ohmic losses of the connection wires. Four main contributions can be identified as discussed in the following.

- The largest contribution to power losses results from the connection wires (R_a). In the experiments these were two thin platinum wires attached to the current collector embedded into the electrodes. The platinum wire has a temperature-dependent resistivity described by Eq. (42). The losses of the wires follow Ohm's law so they are proportional to the cell voltage. At high temperatures, the power loss due to the contact wires is approximately equal to the total peak power of the system.
- The second largest contribution to power losses, amounting to one third of the power output from the system, is due to the ionic resistance of oxygen ions in the dense electrolyte. The ionic resistivity decreases with increasing temperature (Eq. (40)).
- The polarization losses of the anode represent the third largest contribution to power losses and reduces the power of the system by about 10%. Possible causes are slow electrochemical reactions.
- Losses due to the electronic conductivity of the mixed-conducting electrolyte play only a minor role. It is important to note that the electronic current depends strongly on the cell polarization
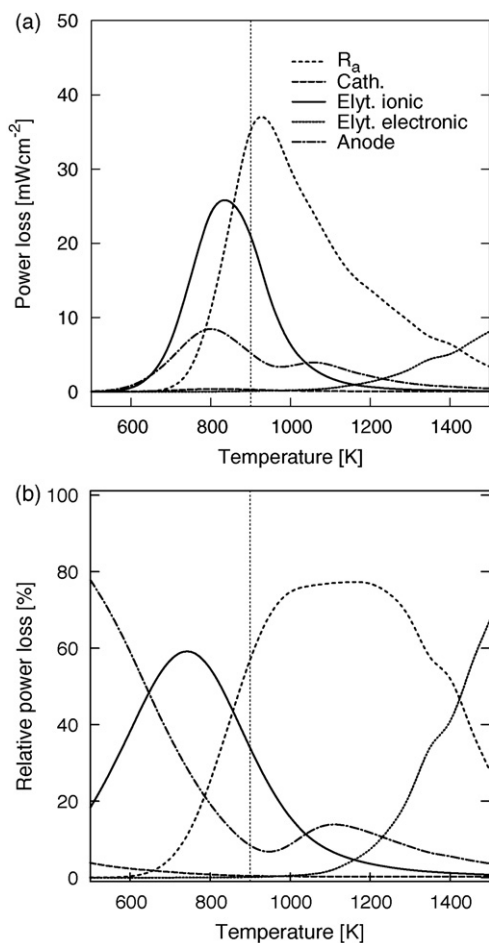
Fig. 8. Calculated power losses of different fuel cell components and processes versus the operating temperature. Simulations are performed for standard conditions using the reduced model. The vertical lines denote the temperature of maximum peak power.

(Eq. (38)): It decreases with increasing polarization. Therefore, although it has a strong impact on the OCV (Fig. 7a), the influence at the actual operating point is rather small. It becomes dominant only at temperatures >1400 K.

The high importance of ohmic losses (connection wires and solid electrolyte) is the reason for the linear behavior of the *IV* curves (Fig. 5).

4. Model-based optimization

The physicochemical model has been shown to reliably predict DFFC performance over a wide range of experimental conditions. We therefore feel confident to use the model for optimizing the design of the DFFC. To this goal, a number of geometrical parameters of the SOFC were varied in order to study their impact on DFFC performance.

Fig. 9 shows the maximum cell power at 900 K versus the thickness of the anode, cathode and electrolyte as well as wire radius. The optimum anode layer thickness (Fig. 9a) is around 20 μm. Reducing the anode thickness from its standard value (175 μm) first results in an increase of power density as the ohmic and gas-phase transport losses decrease. When further reducing anode thickness, the layer becomes too thin to fully support the electrochemical conversion. The thickness of the cathode (Fig. 9b) has almost no influence

on the systems performance. This corresponds to the conclusions drawn in the previous section, where the cathodic contribution to the power loss of the system was insignificant. With decreasing electrolyte layer thickness (Fig. 9c), performance continuously increases, consequently thinner electrolyte layers always reduced the losses. The lower limit would be given by the requirement that the layer must remain gas-tight. Increasing the radius of the connecting wires (Fig. 9d) has the highest impact on the cell performance, allowing an increase of power density by a factor of more than two for wire radii above 1 mm. With further increasing radius there is no further effect because other loss processes become dominant.

The study shows that improvement of cell design allows to increase power density to above 200 mW cm^{-2}, which is significantly higher than the experimentally observed performance of 80 mW cm^{-2} of the base design.

4.1. Summary and conclusions

The direct-flame solid oxide fuel cell (DFFC) is a promising system for power generation in a simple "no-chamber" setup. We have presented a detailed modeling and simulation study of a DFFC operated on methane using a flat-flame burner. A full model was set up comprising an elementary kinetic description of the premixed methane–air flame, a stagnation-point flow description of the coupled heat and mass transport within the gas phase, an elementary kinetic description of the electrochemistry of the SOFC anode, a global kinetic description of the SOFC cathode, as well as heat, mass and charge transport within the SOFC. Simulated current–voltage characteristics show excellent agreement with experimental data published earlier by Kronemayer et al. [10]. Main conclusions are summarized as follows:

- Flame and fuel cell are thermally strongly coupled. Despite strong temperature gradients in the gas phase, the temperature through the fuel cell is almost uniform.
- Flame and fuel cell are chemically decoupled. Fuel cell operation does not affect combustion chemistry.
- Both, H_2 and CO are identified as electrochemically active fuel species.

Due to the high computational effort of the full model, a reduced model was set up for parameter studies. The comparison of simulations with experiments over a wide range of parameters (flame equivalence ratios, burner inflow velocities) showed that all key features of the system were predicted well. Main conclusions are summarized as follows:

- The experimentally observed strong temperature dependence of the DFFC performance is quantitatively reproduced by the model. The system shows an optimum cell temperature of around 900 K.
- Individual contributions of the different loss processes were quantified. Ohmic resistance in the connecting wires and/or the embedded current collectors was found to be the dominant loss process, followed by ionic resistance of the electrolyte.
- Electronic loss currents through the mixed-conducting electrolyte, although important at open circuit, have only a small influence at the actual operating point.

The model was used to study the impact of cell design on performance. An optimum anode thickness was identified. Improved current collection was shown to be of key importance for performance improvement. Based on an optimized cell design, power densities of above 200 mW cm^{-2} can be expected.
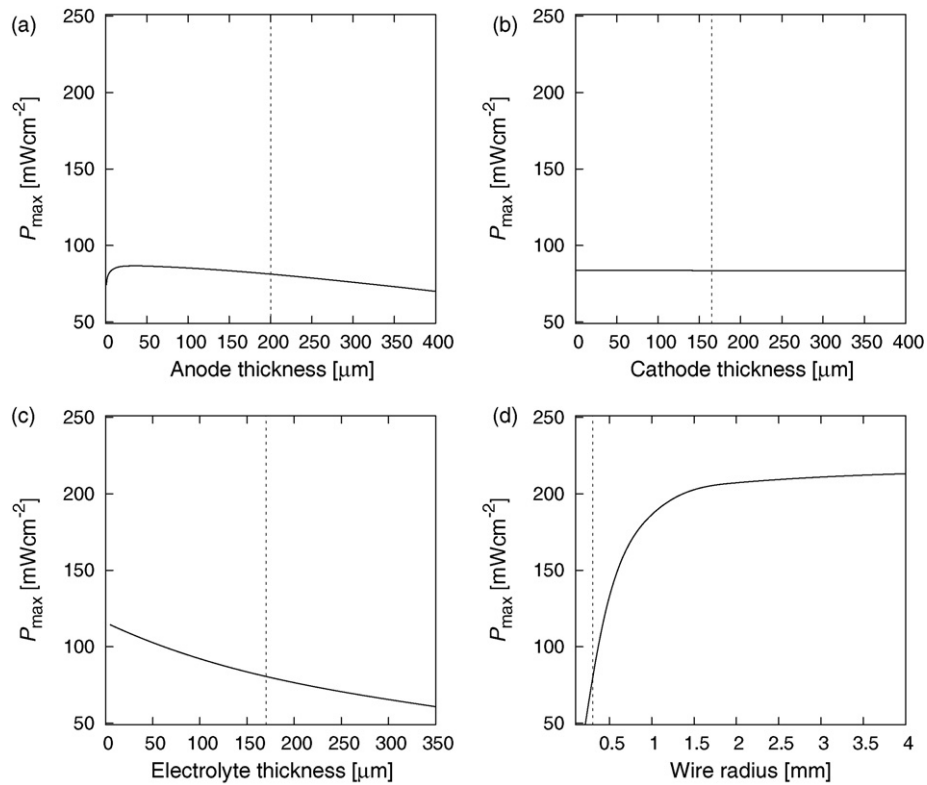
Fig. 9. Maximum power density of the system predicted by the reduced model versus thickness of anode (a), cathode (b), electrolyte layer (c) and radius of the connecting wires (d). The vertical lines indicate the SOFC parameters used in the experimental characterization.

References

[1] Y. Hao, Z. Shao, J. Mederos, W. Lai, D.G. Goodwin, S.M. Haile, Solid State Ionics 177 (2006) 2013–2021.
[2] Z. Shao, S.M. Haile, J. Ahn, P.D. Ronney, Z. Zhan, S.A. Barnett, Nature 435 (2005) 795–798.
[3] T. Hibino, A. Hashimoto, T. Inoue, J. Tokuno, S. Yoshida, M. Sano, Science 288 (2000) 2031–2033.
[4] J.P. Bingue, A.V. Saveliev, A.A. Fridman, L.A. Kennedy, Int. J. Hydrogen Energy 27 (2002) 643–649.
[5] H. Pedersen-Mjaanes, L. Chan, E. Mastorakos, Int. J. Hydrogen Energy 30 (2005) 579–592.
[6] T. Hibino, A. Hashimoto, T. Inoue, J. Tokuno, S. Yoshida, M. Sano, J. Electrochem. Soc. 148 (2001) A544–A549.
[7] M. Horiuchi, S. Suganuma, M. Watanabe, J. Electrochem. Soc. 151 (2004) A1402–A1405.
[8] M. Horiuchi, S. Suganuma, M. Watanabe, Y. Tokutake, in: M. Mogensen (Ed.), 6th European Solid Oxide Fuel Cell Forum, Lucerne, Switzerland, 2004, pp. 154–162.
[9] M. Horiuchi, F. Katagiri, J. Yoshiike, S. Suganuma, Y. Tokutake, H. Kronemayer, W.G. Bessler, J. Power Sources 189 (2009) 950–957.
[10] H. Kronemayer, D. Barzan, M. Horiuchi, S. Suganuma, Y. Tokutake, C. Schulz, W.G. Bessler, J. Power Sources 166 (2007) 120–126.
[11] M. Vogler, D. Barzan, H. Kronemayer, C. Schulz, M. Horiuchi, S. Suganuma, Y. Tokutake, J. Warnatz, W.G. Bessler, ECS Trans. 7 (2007) 555–564.
[12] K. Wang, R. Ran, Y. Hao, Z. Shao, W. Jin, N. Xu, J. Power Sources 177 (2008) 33–39.
[13] W.G. Bessler, S. Gewies, M. Vogler, Electrochim. Acta 53 (2007) 1782–1800.
[14] W.G. Bessler, J. Electrochem. Soc. 153 (2006) A1492–A1504.
[15] R.J. Kee, M.E. Coltrin, P. Glarborg, Chemically Reacting Flow. Theory and Practice, John Wiley & Sons, 2003.
[16] J. Warnatz, U. Maas, R.W. Dibble, Combustion. Physical and Chemical Fundamentals, Modeling and Simulation, Experiments, Pollutant Formation, Springer, Berlin; New York, 2006.
[17] G.P. Smith, D.M. Golden, M. Frenklach, N.W. Moriarty, B. Eiteneer, M. Goldenberg, C.T. Bowman, R.K. Hanson, S. Song, W.C. Gardiner Jr., V.V. Lissianski, Z. Qin, GRI-Mech 3.0. Available from: <http://www.me.berkeley.edu/gri_mech/>.
[18] I. Riess, Solid State Ionics 157 (2003) 1–17.
[19] M. Gödickemeier, L.J. Gauckler, J. Electrochem. Soc. 145 (1998) 414–421.
[20] I. Riess, M. Gödickemeier, L.J. Gauckler, Solid State Ionics 90 (1996) 91–104.
[21] Y. Hao, D.G. Goodwin, J. Electrochem. Soc. 154 (2007) B207–B217.
[22] E.S. Hecht, G.K. Gupta, H. Zhu, A.M. Dean, R.J. Kee, J. Maier, O. Deutschmann, Appl. Catal. A 295 (2005) 40–51.
[23] M. Vogler, A. Bieberle-Hütter, L.J. Gauckler, J. Warnatz, W.G. Bessler, J. Electrochem. Soc. 156 (2009) B663–B672.
[24] H. Zhu, R.J. Kee, V.M. Janardhanan, O. Deutschmann, D.G. Goodwin, J. Electrochem. Soc. 152 (2005) A2427–A2440.
[25] W.G. Bessler, H. Kronemayer, M. Horiuchi, C. Schulz, unpublished data.
[26] M. Gödickemeier, L.J. Gauckler, J. Electrochem. Soc. (1998) 414–421.
[27] S. Gewies, W.G. Bessler, J. Electrochem. Soc. 155 (2008) B937–B952.
[28] V.M. Janardhanan, O. Deutschmann, J. Power Sources 162 (2006) 1192–1202.
[29] VDI-Gesellschaft Verfahrenstechnik und Chemieingenieurswesen (GVC), VDI Wärmeatlas, 4 ed., VDI-Verlag, Düsseldorf, 1984.
[30] S.D. Alaruri, L. Bianchini, A.J. Brewington, Opt. Eng. 37 (1998) 683–687.